Influence of geometry, elasticity properties and boundary conditions on the Mode I purity in sandwich composites

V.N. Burlayenko[a,b,*], D. Pietras[a], T. Sadowski[a]

[a]*Lublin University of Technology, Department of Solid Mechanics, 40 Nadbystrzycka Str., 20-168 Lublin, Poland*
[b]*Department of Applied Mathematics, National Technical University 'KhPI', 2 Kyrpychova Str., Kharkiv 61002, Ukraine*

Abstract

The present work addresses the problem of skin/core debonding in sandwich materials. The main goal is to carry out parametric analyses for studying the influence of various materials, geometrical parameters and boundary conditions of sandwich fracture specimens such as a Single Cantilever Beam and a Double Cantilever Beam on the skin/core opening (K_I) and shearing (K_{II}) modes. The analyses have been performed by means of fracture mechanics tools implemented into the commercial finite element code ABAQUS™. A two-dimensional model of the fracture specimens has been developed with plane strain finite elements. The dependence of the stress intensity factors in the sandwich specimens on the skin thickness, ratio between the Young's moduli of the skin and core materials and boundary conditions imposed on the specimens has been examined under quasi-static loading by using the interaction integral method.

Keywords: sandwich fracture specimens, skin/core interface debonding, bi-material system, fracture parameters, interaction integral method, finite element analysis

1. Introduction

The sandwich composites are widely used in many branches of engineering, especially where there is a demand for the excellent mechanical performance and high bending stiffness at small mass. Moreover, the replacement of the metallic parts of airplanes by their composite counterparts reduces further efforts for their maintenance [1]. A sandwich material usually consists of two stiff skins and a lightweight, soft core. Either homogenous metal sheets or laminated glass or carbon fibre reinforced composites are mainly used as skins, whereas either polymeric or metallic foams with closed or open foam cells are adopted for a core material [2]. In addition, cellular materials produced in the form of honeycomb, folded, lattice and origami-like structures, walls of which can be made of many kinds of materials, are also widely utilized as a core layer [3–5]. The sandwich materials are being developed still for making better their functionality. For instance, the damping and stiffness efficiency and compressive and shear strength and impact resistance of sandwich composites can be improved by the development of new types of the core layer as

suggested in [6–8]. Yet, the interfacial toughness is suggested to be enhanced by modification of the skin/core interface properties, [9].

To provide a safe use of sandwich structural components in real life applications, the properties and behaviour of sandwich materials have to be well predicted. In the literature survey on experimental testing honeycomb and foam cored sandwich materials, different failure modes such as core shear, core crushing, skin wrinkling, skin yielding and skin/core debonding are mentioned, e.g. [10–12]. However, because a variety of material and geometrical properties of sandwich materials tailored for particular applications occurs, sandwich composites are a subject of extensive theoretical research as well. In this regard, beside the analytical solutions, which are usually limited by simple sandwich models, e.g. [13], the finite element (FE) modelling is an efficient tool to predict the behaviour of complex sandwich structures in linear and nonlinear regimes, e.g. [14–19]. In doing so, the data concerning material properties, obtained in laboratory tests are essential to build proper numerical models at meso- or macroscale levels. The other aspect that affects the quality of the FE sandwich models is concerned with the simulation of a microscopically discrete structure of the core. Traditionally, homogenization approaches modelling the core as an equivalent generally anisotropic homogeneous material are used. Some examples of finite element homogenization analyses of sandwich panels can be found in [20–22], and advanced techniques replacing the cores by micropolar continua in simulations are proposed, e.g. in [23, 24].

The main simplification of the mentioned FE models of sandwich composites is an assumption on a perfect bond between the skins (face sheets) and the core. In actual sandwich structures, imperfections at the skin/core interface may cause an appearance of interfacial damage called as debonding. It has already proved by both experimental and theoretical studies that this type of damage results in a reduction of the load bearing capacity [25–27], alterations of modal dynamic properties [28–31] and a modification of overall dynamic responses [32–35] in sandwich structures. Moreover, even a small initial debond may grow and lead to eventual failure of a sandwich structure by debonding. Thus, early detection of such damage in sandwich structures is critical for safety reasons as mentioned in [36–40].

The debonding failure of sandwich composites may be caused by many phenomena, but it is controlled by the strength or fracture toughness of the skin/core interface. In analyses, where a possibility of the skin/core interface failure is taken into account, the interfacial fracture properties are necessary. The theoretical studies on the stress singularity at the crack along the boundary between two dissimilar materials, as is the case of a sandwich material with stiff skins and a lightweight core surrounding the debond, have led to the conclusion that the stress behaviour strongly depends on the mismatch of elastic properties of the interface constituents. This mismatch acts to couple the normal and shear deformations ahead of the crack front. Thus, the interface crack grows in mixed mode conditions [41, 42]. To establish the interface fracture toughness of sandwich materials, appropriate fracture tests should be developed. Since the debonding toughness is minimum in the case of mode I dominant fracture [43], several test methods to measure the interface fracture parameters under mode I conditions realizing peel-dominated loading have been proposed in the literature. Each of those tests differs slightly from another one, and they can be roughly grouped into three configurations: the climbing drum peel test (when the skins are very thin), the double cantilever beam test (DCB) and the single cantilever beam test (SCB), e.g. [44–48]. The review of data reduction methods used for defining the fracture parameters from the tests can be found in [49].

In most studies on critical debonding toughness, an uncertainty about the mode I purity and the specimen geometry dependence are reported, e.g. in [43]. Also, the experimental findings

2

do not enable to test a huge variety of sandwich configurations existing in-service. Additionally, the test data show remarkable scatter in reported debonding toughness values for given sandwich systems [50]. Thus, a correlation between the various kinds of fracture scenarios under mode I loading and the specimen geometry, fixtures and material constituents is not well understood yet. In this respect, parametric theoretical studies become indispensable to estimate the required fracture parameters of sandwich materials.

Although a number of analytical solutions exists for bi-material interface cracks, such solutions are often infeasible for dealing with a complex geometry and complicated boundary and loading conditions that exist in the test methods of interest. Meanwhile, fracture mechanics-based tools implemented into commercial finite element analysis codes, such as ABAQUS™, ANSYS®, MSC Marc®, and so on enable to make simulations of skin/core debonding, e.g. [51–55]. The accuracy, however, of such predictions depends essentially on the reliability of both fracture data such as debonding toughness and fracture parameters such as the strain energy release rate (SERR) and phase angle or the stress intensity factors (SIFs) being calculated during the analysis. The parameters are used as an input in appropriate fracture criteria. Therefore, a clear motivation of the current work occurs for estimating a degree of mode I dominance and its dependence on geometry and material property mismatch to adequately characterize skin/core debonding in popular sandwich DCB and SCB test methods. For this purpose, the ABAQUS code [56] is used to evaluate SIFs in the both types of sandwich specimens. The materials of skins and core of the specimens are treated at the mesoscale level by omitting their discrete internal microstructure and are assumed to be isotropic homogeneous with different elastic constants. A two-dimensional (2-D) model of the fracture specimens accounting for a general stress state at the tip of debonding is developed with plane strain finite elements available in the code. The SIFs for a skin/core bi-material interface crack are defined by using the interaction integral method, which is a built-in option of ABAQUS, then the SERR and the phase angle are computed using the interface fracture mechanics approach. The variations of mode I percentage relatively geometry and material properties in the sandwich specimens are identified through extensive parametric studies. These numerical findings are thought will be helpful for producing reliable values of debonding toughness in sandwich composites for a wide variety of skin/core configurations.

2. Theoretical and Computational Background

In practical engineering problems, a broad range of structures is undergone fracturing in which bi-material interface crack problems prevail over homogeneous ones. Composite sandwich materials are typical examples of bi-material interface cracking. For the sake of completeness, the linear elastic fracture mechanics (LEFM) approach used to state an interface bi-material crack problem in the extent necessary for the present work is briefly considered below. In this section, we follow the notations presented in [41, 57].

2.1. 2-D bi-material interface crack

For each material pair, Fig. 1, singular stress and displacement fields exist at the bi-material crack tip according to the assumptions of LEFM. Following [41, 57], in an elasticity plane problem, the near-tip stress fields at a point located at a distance r and an angle θ from the crack tip can be presented in the form:
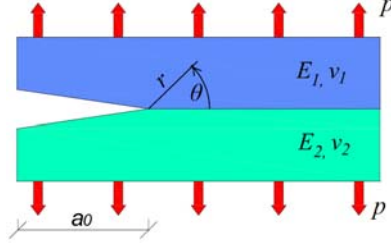
3

Figure 1: Crack at a bi-material interface.

$$\sigma_{mn}(r, \theta) = \frac{1}{\sqrt{2\pi r}} \left\{ \Re e \left[K r^{i\epsilon} \right] \tilde{\sigma}_{mn}^{I}(\theta, \epsilon) + \Im m \left[K r^{i\epsilon} \right] \tilde{\sigma}_{mn}^{II}(\theta, \epsilon) \right\}, \tag{1}$$

where $(m, n) = (1, 2)$ for the Cartesian coordinates (x_1, x_2) or $(m, n) = (r, \theta)$ for the polar coordinates; $K = K_1 + iK_2 = |K| e^{i\psi}$ is the complex interface stress intensity factor with K_1 and K_2 used instead of K_I and K_{II} adopted for homogeneous materials; $\tilde{\sigma}_{mn}^{M}$ with $M = I, II$ are universal angular functions in polar or Cartesian coordinate systems centred at the crack tip; ϵ is the oscillation index depending on elastic mismatch parameters:

$$\epsilon = \frac{1}{2\pi} \ln \left(\frac{1 - \beta}{1 + \beta} \right) \tag{2}$$

Here, β is the second Dundurs' mismatch parameter defined by the shear moduli G_k, Poisson's ratios ν_k and Kolosov constants $\kappa_k = 3 - 4\nu_k$ in plain strain and $\kappa_k = (3 - \nu_k)/(1 + \nu_k)$ in plane stress of the two materials $k = 1, 2$ as follows:

$$\beta = \frac{G_1(\kappa_2 - 1) - G_2(\kappa_1 - 1)}{G_1(\kappa_2 + 1) + G_2(\kappa_1 + 1)} \tag{3}$$

With K_1 and K_2 as the components of the complex interface SIF and following from (1), the local stress field in the interface a distance r ahead of the crack tip is given by [57]:

$$(\sigma_{22} + i\sigma_{12})_{\theta=0} = \frac{(K_1 + iK_2) r^{i\epsilon}}{\sqrt{2\pi r}} \tag{4}$$

The stresses in (4) oscillate as the crack tip is approached. To avoid oscillations in the mode mixity parameter, $\psi = \tan^{-1}(\sigma_{12}/\sigma_{22})$, a characteristic length scale $\hat{l}$ is introduced as discussed in [42]. Then, the non-oscillatory phase angle $\hat{\psi}$ is established as follows:

$$\hat{\psi} = \tan^{-1} \left(\frac{\sigma_{12}}{\sigma_{22}} \right) \bigg|_{r=\hat{l}} = \tan^{-1} \frac{\Im m[K\hat{l}^{i\epsilon}]}{\Re e[K\hat{l}^{i\epsilon}]} \tag{5}$$

Using the length scale parameter $\hat{l}$, a normalized complex interface SIF with ordinary units of the SIF in homogeneous materials can be used in the form: $K\hat{l}^{i\epsilon} = \hat{K}$. Herewith, the amplitude of $\hat{K}$ is identical to K, but its phase angle is shifted with respect to ψ as $\hat{\psi} = \psi + \epsilon \ln \hat{l}$.

Also, the SERR is used for characterizing the interfacial strength as an alternative to the components of the complex interface SIF. With K and its complex conjugate value $\bar{K}$, the SERR can be expressed in the form [42]:
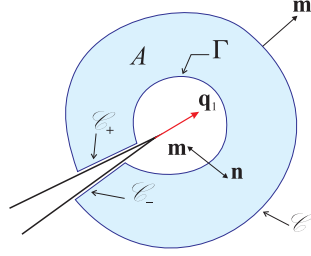
4

Figure 2: A closed contour $C \cup C_+ \cup \Gamma \cup C_-$ encloses a domain A that includes the crack-tip region as $\Gamma \to 0$.

$$\mathcal{G} = \frac{1/E_1^* + 1/E_2^*}{2\cosh^2 \pi\epsilon} K\bar{K} = \frac{1}{H}(K_1^2 + K_2^2), \tag{6}$$

where $1/H = (1/E_1^* + 1/E_2^*)/2\cosh^2 \pi\epsilon$ with the Young's moduli $E_k^* = E_k$ in plane stress and $E_k^* = E_k/(1 - \nu_k)$ in plane strain for the materials $k = 1, 2$.

2.2. Interaction integral method

In the present study, the interaction integral method (IIM) [58] implemented into the ABAQUS code is used to determine the stress intensity factors K_1 and K_2 for DCB and SCB sandwich specimens with the skins and the core made of dissimilar homogeneous isotropic materials as shown in Fig. 1. Following [59], the 2-D interaction integral for a straight crack along the x_1-axis for any of fracture modes $M = 1, 2$ can be presented as

$$I_M = -\oint_{C+C_++\Gamma+C_-} \mathbf{m} \cdot \mathbf{Q}_M \cdot \mathbf{q}_1 d\Gamma, \tag{7}$$

with the integrand $\mathbf{Q}_M$ given by the expression

$$\mathbf{Q}_M = \boldsymbol{\sigma} : (\boldsymbol{\varepsilon})_M^{aux} \mathbf{I} - \boldsymbol{\sigma} \cdot \left(\frac{\partial \mathbf{u}}{\partial x_1}\right)_M^{aux} - (\boldsymbol{\sigma})_M^{aux} \frac{\partial \mathbf{u}}{\partial x_1}, \tag{8}$$

where $\mathbf{q}_1(\mathbf{x})$ is a smooth weighting function within the region enclosed by the contour $C \cup C_+ \cup \Gamma \cup C_-$, which takes one on Γ and zero on C; $\mathbf{m}$ is an outward unit normal to the domain enclosed by this contour such that $\mathbf{m} = \mathbf{n}$ on C, $\mathbf{m} = -\mathbf{n}$ on Γ, $\mathbf{m} = +1$ on C_- and $\mathbf{m} = -1$ on C_+, as shown in Fig. 2; $\boldsymbol{\sigma}, \boldsymbol{\varepsilon}$ and $\mathbf{u}$ are stress, strain and displacement fields, respectively; the superscript $'aux'$ means auxiliary crack-tip fields adopted for pure either Mode I or Mode II; the limit $\Gamma \to 0$ indicates that shrinks onto the crack tip.

Then, by evaluating the interaction integral I_M, where the auxiliary crack-tip fields are assumed to be asymptotic Williams type solutions of corresponding material system regardless of an actual geometry, the SIFs of an interface crack between two dissimilar materials are determined as follows:

$$K_M = \frac{H}{2K_M^{aux}} I_M \tag{9}$$

In the FEM context, the interaction line integral (7) is usually converted into a domain formulation. ABAQUS uses the virtual crack extension method [60] to calculate the interaction integral, whose a domain form is given by
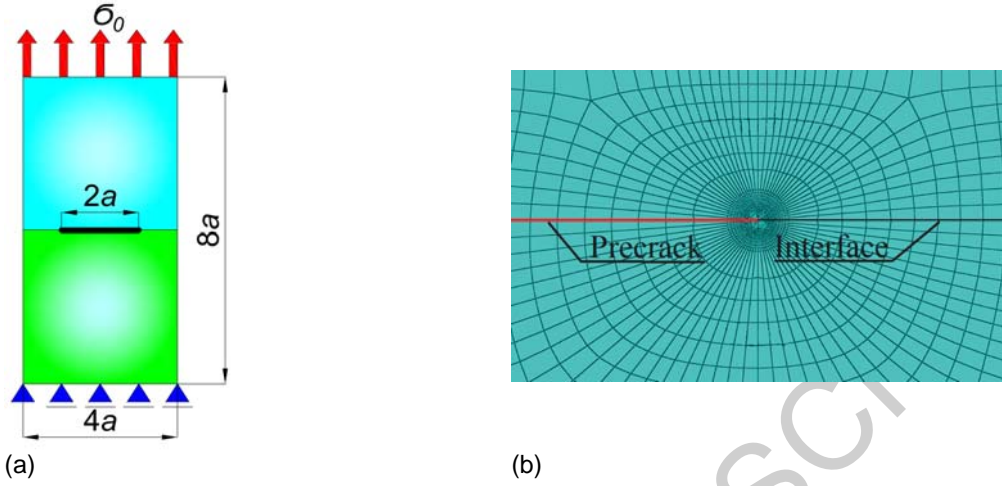
5

Figure 3: A centre cracked plate under tension: (a) geometry, boundary and loading conditions; and (b) a mesh refinement in the vicinity of the right crack tip.

$$I_M = \int_A \mathbf{Q}^M : \frac{\partial \mathbf{q}_1}{\partial \mathbf{x}} dA, \tag{10}$$

where A is the domain enclosed by the contour $C \cup C_+ \cup \Gamma \cup C_-$ as illustrated in Fig. 2. The domain integral calculation is performed by defining a group of finite elements forming a ring around the crack tip. The numerical calculation is achieved using element by element integration of the results of a finite element analysis with the Gaussian quadrature. Finally, the total result is a summation over all the elements belonging the domain A. More details concerning the computational implementation of the IIM into the ABAQUS software can be found in [56].

3. Numerical results

In this section, we present the results of calculations of the SIFs K_1 and K_2 of bi-material interface cracks in SCB and DCB sandwich specimens using the finite element analyses in conjunction with the interaction integral method as described in Section 2.2.

3.1. Convergence studies

At the beginning, the mesh study analysis is performed. As a reference, the results obtained in [61] for a bi-material plate with central crack subjected to tension stress $\sigma_0 = 1$ MPa are considered as shown in Fig. 3a. The parameter a was equal to 0.5 mm. The elastic properties of each material of the plate are assumed to be linear isotropic with known Young's moduli, E_i and Poisson's ratios, ν_i, where $i = 1, 2$. In the calculations, the two ratio of moduli $E_1/E_2 = 2, 10$, but the same $\nu_1 = \nu_2 = 0.3$ have been used. The 2-D rectangular plate was discretized using 8-node isoparametric plane strain elements CPE8 available in ABAQUS, [56]. The interfacial center crack was modeled by duplicate nodes between finite elements placed along the crack faces. The near-tip regions were covered by "spider-web" mesh with at least of 10 rings of elements surrounding the crack tip. The circumference of each ring was divided into 80 equal

6

Table 1: Results of the FEM mesh study

E_1/E_2	No	d	K_1^*	Δ_{K_1}, % [1]	K_2^*	Δ_{K_2}, %
	1	0.40	1.232	4.495	0.058	5.172
	2	0.20	1.178	0.085	0.054	1.852
2	3	0.10	1.178	0.085	0.054	1.852
	4	0.05	1.178	0.085	0.050	0.000
	5	0.4	1.179	4.987	0.133	7.519
10	6	0.2	1.232	9.706	0.123	0.000
	7	0.1	1.123	0.000	0.123	0.000

[1] $\Delta = \frac{|Ref - FEM|}{Ref} \times 100\%$ with 'Ref' as reference values given in [61]

sized segments as illustrated in Fig. 3b. The non-dimensional mesh size parameter d defined by a ratio between the mesh eye dimension d_m and the crack length a, i.e. $d = d_m/a$ is used to characterize the mesh refinement similarly to [62]. To introduce the square-root singularity required within the LEFM, the quarter point singular elements have been inserted into the mesh in the vicinity of the crack tip. Stress intensity factors K_1 and K_2 extracted using the IIM have been normalized by a factor:

$$K_i^* = \frac{K_i}{\sigma_0 \sqrt{\pi a}}$$

As known, the dimensions of K_i are stress units times length units raised to power $(1/2 - i\epsilon)$ [42]. Throughout this paper, the units of K_i are omitted implying that an appropriate normalization by the characteristic length $\hat{l}$ has been carried out. The results of seven different calculations and their relative errors with respect to the reference values [61] are listed in Table 1. One can see that starting from $d = 0.2$ a very good agreement between the computed and reference SIFs occurs, and the numerical results converge to the reference ones with mesh refinement. Based on this study, the finite element mesh with the refinement parameter $d = 0.05$ has been used in all further SIF predictions of the sandwich specimens.

3.2. Geometry and mechanical properties of the sandwich system

As mentioned in Introduction, since there is an indeterminacy of choice of the test method for better characterizing the Mode I skin/core debonding in sandwich composites [43], the Mode I purity of popular interlaminar fracture toughness sandwich DCB and SCB specimens is numerically estimated through a virtual testing with 2-D finite element models. The study aimed to examine whether any of the test configurations is in pure opening mode or if the mode mixity plays an important role under the test conditions. Fig. 4a presents a general geometry of the sandwich samples analysed in this paper. Since the skin (or face sheet) thickness, modifying the geometry of SCB and DCB samples, has a high impact on the values of SERR in the both fracture specimens [48], the variation of the skin thickness is chosen as a major parameter in the numerical studies. Moreover, for each the test method, the following parameters have also been varied in the calculations:

- the length of initial skin/core debonding (pre-crack), a_0,

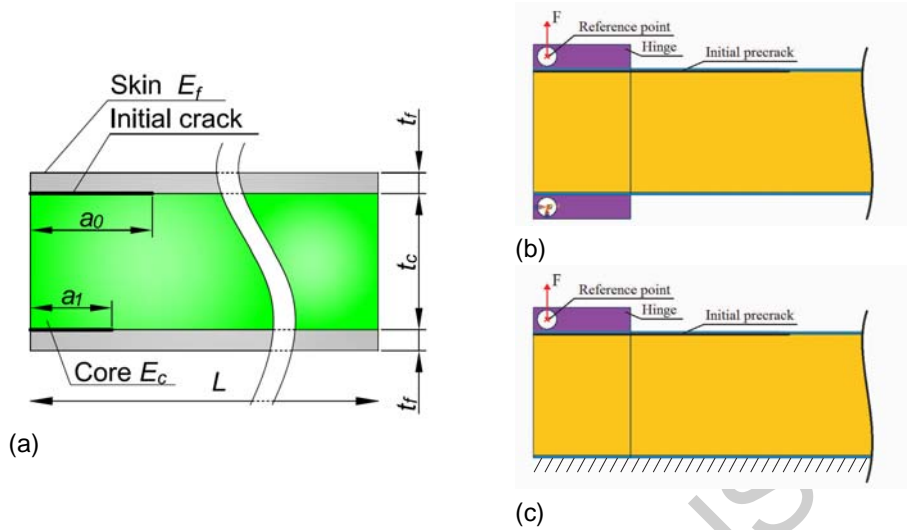- the type of bi-material skin-to-core configuration, E_f/E_c.

7

Figure 4: Sandwich samples considered in the analyses: (a) a general geometry; (b) loading in the DCB test; and (c) loading in the SCB test.

Table 2: Material properties of the sandwich specimens.

Constituents	Material constants
PVC foam core	$E_c = 80$ MPa and 250 MPa; $\nu_c = 0.25$
Composite skin	$E_f = E_{xx} = 25$ GPa; $\nu_f = \nu_{xz} = 0.325$
Aluminum skin	$E_f = 69.5$ GPa; $\nu_f = 0.3$

The specimens of length of L=250 mm and width of b=25 mm with the thickness of core of t_c=25 mm and the thicknesses of skins, t_f ranging from 0.1 mm to 4.1 mm by increment 0.2 mm and 5.1,6.1 and 10.1 mm have been analysed. To capture non-linear effects related to the deformation of specimens with thin skins, geometrically non-linear finite element analyses have been performed. For all the models, four lengths of initial debonding such as a_0=50,70,90 and 110 mm have been considered. The strategy of finite element meshing with refinement at the crack tip region, described in Section 3.1 was adopted for discretization of the sandwich specimens. Also, the analyses were performed for two different skin materials such as glass/epoxy laminated composite and aluminium, and two core materials presenting a polyvinyl chloride (PVC) foam of different densities. In doing so, linear elastic isotropic properties were assumed for all the sandwich constituents. In the case of orthotropic material it was assumed that the principal material axes are aligned with the global coordinate system, where the x-axis is directed along a longitudinal direction of the specimen. The mechanical properties of the core and the skins, which are typically used in a wide range of engineering applications, are shown in Table 2, where the material constants were taken from manufactures' data.

As known from the actual fracture test methods, the transverse force, F acts on the top skin of both DCB and SCB specimens via a steel hinge as shown in Figs. 4b and 4c, respectively. To accurately reproduce this loading conditions in finite element models of the specimens, the TIE constrains were used to link the hinge, modelled as a rigid bogy, with the debonded face

8

sheet of the sandwich beams. Moreover, the concentrated force was applied to a reference point given at the centre of the hinge hole. The point was connected to the hole edge using Multi Point Constraints (MPC). This type of constraints allows rotating the hinge relatively to the point where the force is applied that simulates the real conditions of the laboratory tests. The same constraints were also imposed in the hinge bonded to the bottom skin of the DCB specimen to provide appropriate boundary conditions at the second reference point (Fig. 4b), whereas the bottom skin of the SCB specimen was subjected to the ENCASTRE type of constraints (Fig. 4c).

The influence of possible imperfections that might actually happen during the DCB and SCB tests such as an appearance of debonding at the bottom intact skin/core interface of the DCB specimen or a violation of fixture of the bottom skin to the base in the SCB specimen on a purity of Mode I state is also examined in those specimens. In the case of the DCB sample, the second debonding of length of a_1 was introduced into the model at the bottom skin/core interface (Fig. 4a), whereas the boundary conditions applied to the bottom skin were only changed for the SCB model (Fig. 4c). Three lengths of the second debonding equal to 20,35 and 50 mm (Fig. 21) and five lengths of the imperfect fixture equal to 5,12.5,25,37.5 and 50 mm (Fig. 12) have been analysed.

3.3. Sandwich Single Cantilever Beam (SCB) test specimen

First, a single cantilever beam sandwich specimen is modelled. The configuration of the SCB test with given boundary conditions and scheme of loading is illustrated in Fig 5. The overall purpose of the test is to measure the static debonding toughness associated with peeling the skin from the core in sandwich materials. An upward force, F applied to the specimen through a steel hinge mounted on the upper debonded face sheet was taken as a unit load in all the cases, while the lower intact face sheet was affixed to a rigid base.
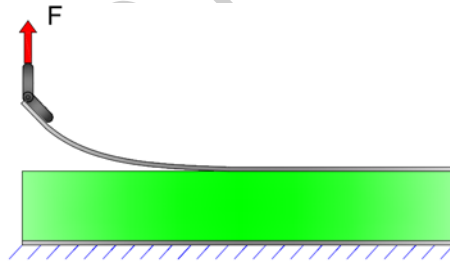

Figure 5: Sandwich Single Cantilever Beam test specimen.

An approximate estimation of the total SERR, $\mathcal{G}^{SCB}$ based on the elastic foundation analysis of a SCB sandwich sample can be presented as [50]:

$$\mathcal{G}^{SCB} = \frac{F^2}{2b^2} \left\{ \frac{12}{E_f h_f^3} (a_0^2 + 2a_0 \eta^{1/4} + \eta^{1/2}) \right\}, \tag{11}$$

where the parameter is given by $\eta = bh_f^3 E_f/(3k)$ with elastic foundation coefficient accepted as $k = 2bE_c/h_c$. The expression (11) is used along with the LEFM formula (6) for comparative purposes in the calculations of the SERR. The results of comparison, presented as relative errors between FEM and analytic data $\Delta \mathcal{G} = \frac{|\mathcal{G} - \mathcal{G}^{SCB}|}{\mathcal{G}} \times 100\%$, which are scattered along corresponding linear trend lines depending on the skin thickness, for the SCB specimen with the core modulus

9

E_c=80 MPa and with composite and aluminium skins, are plotted in Fig. 6 for different pre-crack lengths. The analytic formula (11) overestimates the SERR, especially for short pre-cracks, but it was no more than 50% in our study. Herewith, the aluminium-PVC configuration with higher E_f/E_c ratio gave bit larger differences than those in the composite-PVC configuration with lower E_f/E_c ratio. Also, the errors were less for longer pre-cracks and thicker skins.
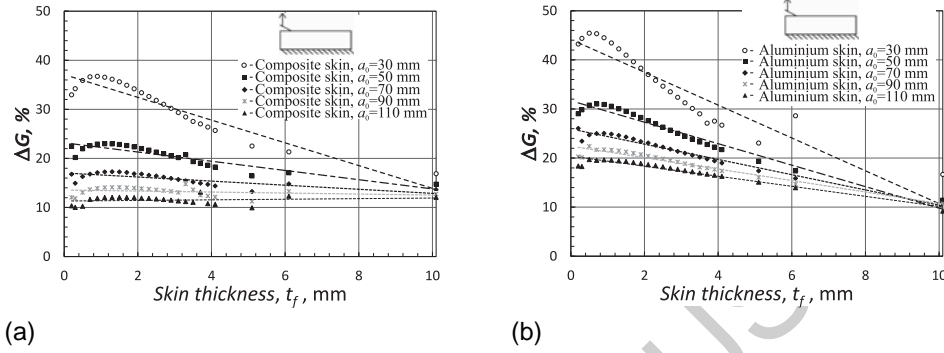

(a)

(b)

Figure 6: The variation of relative errors $\Delta\mathcal{G}$ vs. the skin thickness t_f for different pre-crack lengths in the SCB test with: (a) composite skin; and (b) aluminium skin.

In order to ensure the confidence in the finite element models, developed for the SCB sandwich specimen, the comparison of finite element predictions of the SERR over a range of crack lengths to experimental data available in the literature is carried out. SCB specimens tested in [44] as tilted sandwich debond (TSD) samples at the zero tilt angle have been selected for this purpose. Mechanical properties and dimensions of those specimens and other experimental details may be found in the original reference. Fig. 7 illustrates the deviation observed between the finite element analysis and experimentally obtained SERR at different pre-crack lengths. It should be noted that a dimensionless SERR normalized by $\mathcal{G}^* = \mathcal{G} \times E_f h_f^3/(Fb)^2$ is presented in the plot. A quite good correlation between the numerical and experimental data can clearly be seen. This certainly confirms that the computational models used for modelling the behavior of SCB sandwich specimens provide high fidelity results.
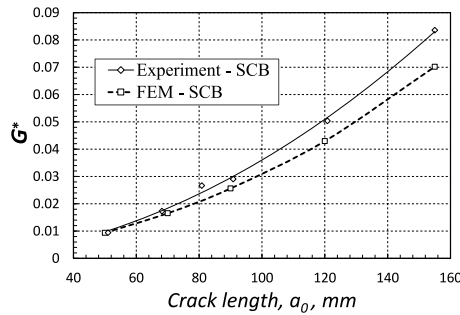

Figure 7: Comparison between numerical and experimental SERRs vs. crack length for SCB sandwich specimens.

Further a series of analyses was conducted to examine the effect of the skin thickness, length of initial debonding and bi-material configuration on the fracture parameters. The results of
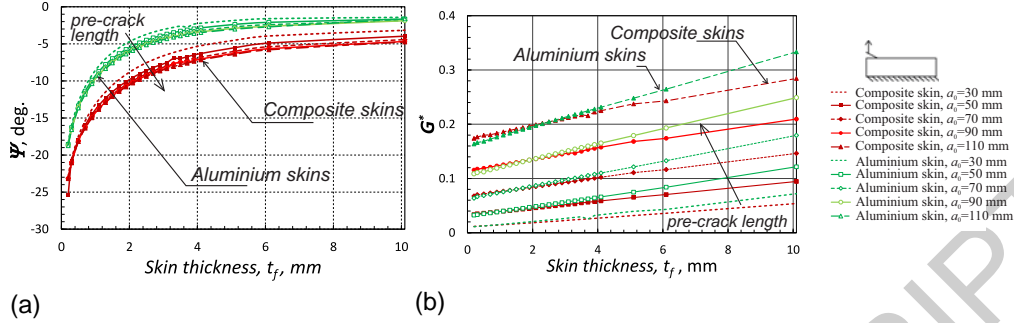
10

Figure 8: The variation of fracture parameters vs. the skin thickness t_f at different pre-crack lengths in the SCB test: (a) the phase angle $\hat{\psi}$ vs. t_f; and (b) the normalized SERR $\mathcal{G}^*$ vs. t_f.

parametric studies, presented by curves of the phase angle $\hat{\psi}$ and the normalized SERR $\mathcal{G}^* = \mathcal{G} \times E_f h_f^3/(Fb)^2$ that were extracted from the FEM predictions using the IIM and formula (5) and (6), respectively, versus the skin thickness at different pre-crack lengths for both the composite-PVC and aluminium-PVC material combinations with the core modulus E_c=80 MPa are shown in Fig 8. The results indicate that the Mode I purity in this test is strongly dependent on the skin thickness. Particulary, for the skin thicknesses ranging from 0.1 to 1.7 mm the phase angle is within $(-26°, -10°)$ for both the material combinations, i.e. a substantial contribution of the mode II occurs. Thus, such the SCB specimen geometry is less appropriate for estimating the fracture toughness of the skin/core interface in mode I loading. Meantime, medium and relatively thick skins provide mode I dominated conditions in this test method. The curves visible in Fig 8a asymptotically tend to small non-zero values of $\hat{\psi}$ with increasing the skin thickness that is a gradual increase of mode I dominance is observed. Those saturation values are slightly higher for longer pre-cracks. Herewith, the specimens with aluminium skins (higher skin modulus E_f) produce better conditions of mode I dominant debonding. It also is evident that the phase angle is negative over all the range of skin thicknesses regardless the skin/core material compositions. That is the SCB design provides debonding propagation directed toward the skin, but as the skin is usually stiffer than the skin/core interface, the crack will tend to grow along the interface. Another result obtained for the SCB test is that the SERR linearly increases with increasing the skin thickness and the SERR is higher for longer pre-cracks. Also, the specimens with stiffer aluminium skins induce higher level of the SERR compared to the specimens with composite skins. Yet, the difference between the SERR values of thin (up to around 3.9 mm) aluminium and composite skins is small, but it becomes larger with increasing the skin thickness.

The variations of phase angle and normalized SERR with increasing the pre-crack length at different skin thicknesses are shown in Fig 9. It is evident that at each the skin thickness for both the bi-material configurations, the phase angle is almost insensitive to the initial cracks except at a very short ones (up to 50 mm), while the SERR increases with growing the pre-crack length. Herewith, for most the skin thickness, the lines in the plots are similar to each other, i.e any of them could be obtained by shifting the curve in the ordinate direction. This shows that the mode mixity ratio remains stable during the crack propagation in the SCB test at least for the range of skin thicknesses and pre-crack lengths considered.

The effect of the core rigidity on the phase angle and the SERR is illustrated in Fig. 10. The specimen with the composite skins and a core modulus taken as E_c=250 MPa was analysed. As seen in the plots, the phase angle is higher for the stiffer core, i.e increasing E_c causes a bigger
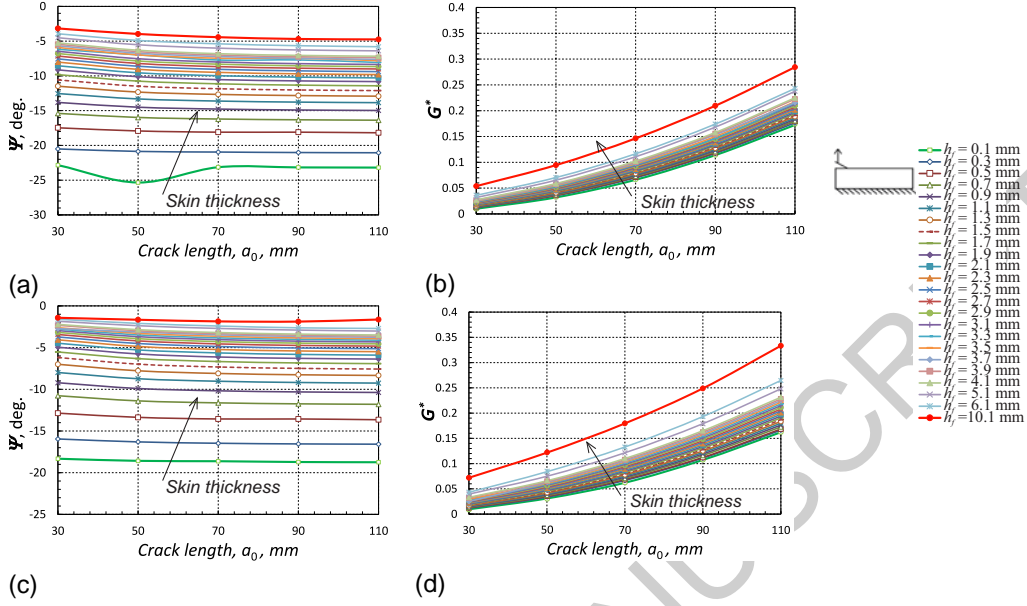
11

Figure 9: The variation of phase angle $\hat{\psi}$ and normalized SERR $\mathcal{G}^*$ vs. the pre-crack length a_0 at different skin thicknesses in the SCB test with: (a)-(b) composite skin; and (c)-(d) aluminium skin.

deviation away from mode I state. Also, the stiffer core results in a lower level of the SERR due to smaller deformations in such the core. However, the variations of phase angle and SERR with respect to skin thickness and pre-crack length keep trends similar to those for the low modulus core. Thus, the SCB test is able to provide a mode I dominance for both soft and stiff core materials.

Of particular interest was also the distribution of near-tip stress fields associated with skin/core debonding. Fig. 11 presents the contour plots of stresses in the vicinity of the crack tip of debonding of $a_0 = 50$ mm for the SCB specimen with the composite skins of thickness of h_f=2.0 mm and the core modulus of E_c=80 MPa. The form of stress distributions for all other skin/core geometrical and material conditions of the SCB test was similar to the presented one and distinguished from it only in the stress level induced. The analyses showed that the maximum longitudinal normal stresses are mainly developed in the upper skin due to its high in-plane and bending resistance, Fig. 11a, whereas the transverse normal stresses are biggest in the region around the crack tip, Fig. 11b. Also at the crack tip, the shear stresses exist for any design of the SCB specimen, Fig. 11c. However, they are smaller about one order of magnitude than the transverse normal stresses in the same region. Despite these relatively small magnitudes, the sign of shear stresses in the vicinity of the crack tip defines the orientation of presumed crack growth direction [43]. As seen in Fig. 11c, the shear stresses developed in the area around the crack tip are negative that confirms the findings observed above for $\hat{\psi}$ and $\mathcal{G}$ postulating the crack propagation either into the skin material or along the skin/core interface in the SCB test.

Numerical studies were also performed to find out how the mode I purity of the SCB specimen changes, when insufficient support conditions are realized in the test. A modified SCB test design is presented in Fig. 12, where the bottom part of the sample is partially fixed to the base. The parametric studies of the SCB specimen with pre-crack of a_0=50 mm and the core modulus
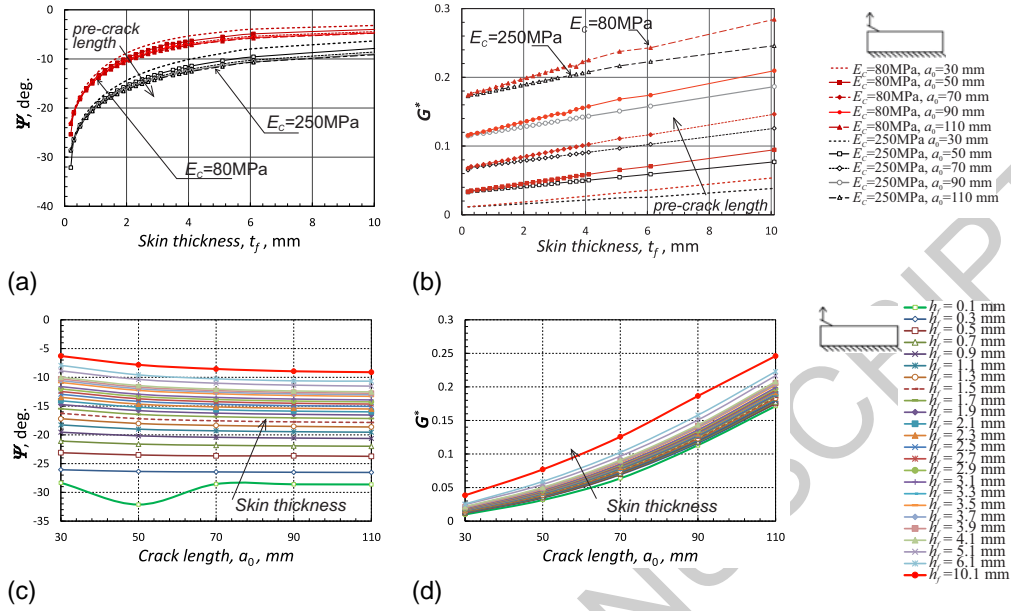
12

Figure 10: The variation of fracture parameters in the SCB specimen with composite skins and core modulus E_c=250 MPa: (a) the phase angle $\hat{\psi}$ vs. t_f; (b) the normalized SERR $\mathcal{G}^*$ vs. t_f; (c) the phase angle $\hat{\psi}$ vs. a_0; and (d) the normalized SERR $\mathcal{G}^*$ vs. a_0.
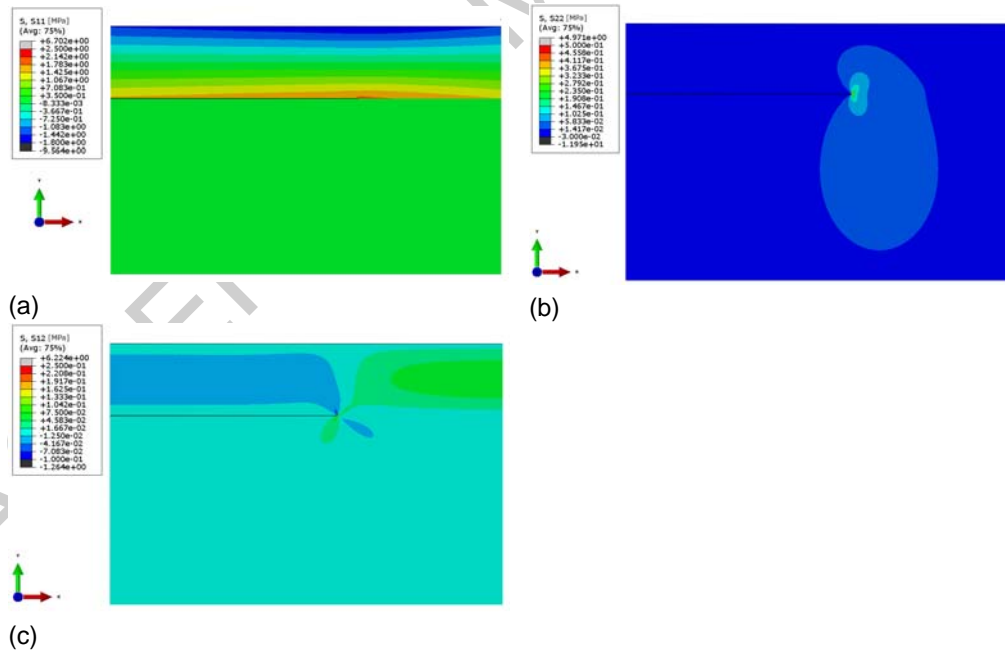

Figure 11: Stress distribution in front of the debonding in SCB specimen: (a) longitudinal normal stress σ_{11}; (b) transverse normal stress σ_{22}; and (c) in-plane shear stress σ_{12}.
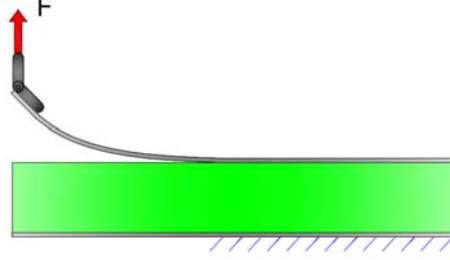
13

Figure 12: Modified sandwich SBC test specimen.

E_c=80 MPa at different support imperfections are conducted and the results are illustrated in Fig. 13. Analysing the plots from the mode mixity standpoint, one can see that the short imperfections, extending up to a half of the pre-crack, have no significant influence on the phase angle for all the range of skin thicknesses in both the types of bi-material configurations. Unlike this the longer imperfections remarkably change the behaviour of the mode mixity parameter. It takes larger negative values compared to the standard SCB test with increasing the skin thickness, i.e. mode I component decreases, but mode II drastically increases. It is interesting that the SERR is not influenced much by all the imperfection lengths in the case of thin skins, but it decreases with increasing the length of imperfect fixture at thicker skins. This is due to the change in mode mixity as mentioned above, especially for the specimens with stiffer aluminium skins, Fig. 13d. Herewith, the differences in the SERR values between the standard and imperfect specimens become to be more evident at the skin thickness of around h_f=2.0 mm for both the composite and aluminium skins as seen in Fig. 13b and d, respectively. This indicates an increasing role of the bending rigidity of thicker skins. Thus, a partial release of the clamped skin in the SCB test leads to more negative phase angle, i.e. smaller mode I dominance and larger contribution of mode II component. The latter becomes more profound for thicker and stiffer skins.

3.4. Sandwich Double Cantilever Beam (DCB) test specimen

A schematic of the DCB test method is illustrated in Fig. 14. In this test, the same piano hinges like in the SCB test are usually used. The DCB specimen is subjected to an opening displacement by applying to the grip plates of the hinges either two opposite transverse loads (Fig. 14) or an up-ward load and boundary constraints (Fig. 4b). The asymmetry of the specimen, with the lower leg being more rigid in flexure than the upper one may result in a slight rotation of the specimen at large opening displacements, but usually such a rotation tends to be small in actual tests [46].

The total SERR of the sandwich DCB specimen can be analytically evaluated using the elastic foundation analysis as follows [46]:

$$\mathcal{G}^{DCB} = \frac{F^2}{2b^2} \left\{ \frac{1}{G_{xz}h_c} + \frac{a_0^2}{(D - B^2/A)} + \frac{12}{E_f h_f^3}(a_0^2 + 2a_0\eta^{1/4} + \eta^{1/2}) \right\}, \tag{12}$$

where the parameter η and the foundation coefficient k are identical to those in (11); and the stiffnesses A, B and D are calculated as

$$A = E_f h_f + E_c h_c, \ B = h_f h_c (E_c - E_f)/2 \text{ and } D = \frac{1}{12} \left\{ E_f(h_f^3 + 3h_f h_c^2) + E_c(h_c^3 + 3h_f h_c^3) \right\}$$
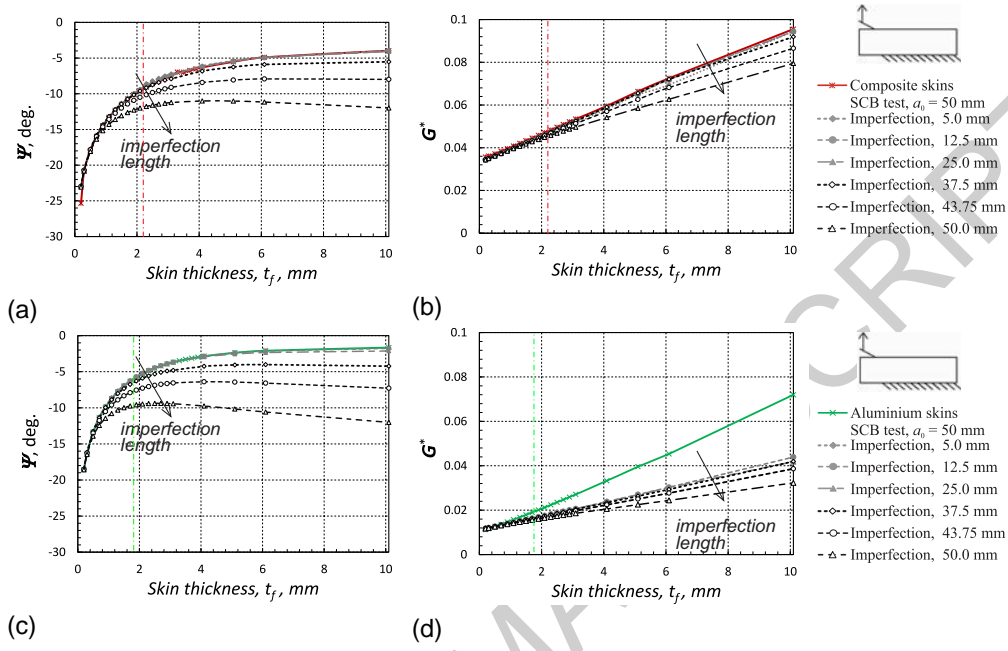
14

Figure 13: Comparisons of the phase angle and the normalized SERR vs. the skin thickness t_f between standard and modified SCB tests: (a)-(b) composite skins; and (c)-(d) aluminium skins.
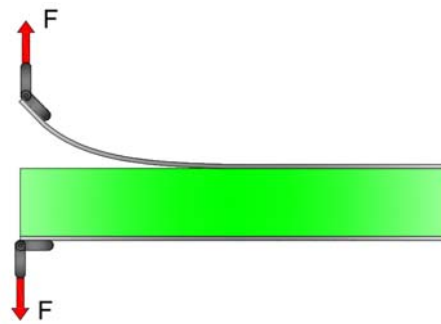

Figure 14: Sandwich Double Cantilever Beam test specimen.

15

Fig. 15 shows the results of comparison of the SERR for different skin thicknesses obtained by the FEM calculations based on the IIM in conjunction with the formula (6) and computed using the approximate analytic expression (12). Although the analytical results overestimate the numerical ones, the differences (relative errors $\Delta \mathcal{G}$) between them do not exceed 50% and are smaller for longer pre-cracks, thicker skins and lower E_f/E_c ratios. This is analogous to the results observed for SCB specimens considered in Section 3.3.
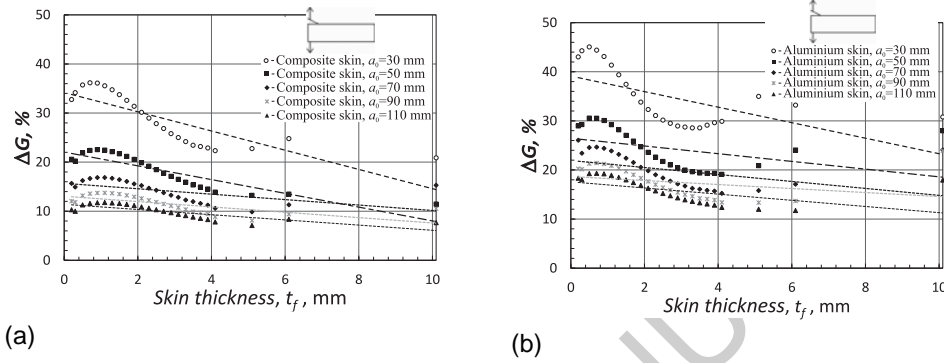

Figure 15: The variation of relative errors $\Delta \mathcal{G} = \frac{|\mathcal{G}-\mathcal{G}^{DCB}|}{\mathcal{G}} \times 100\%$ vs. the skin thickness t_f for different pre-crack lengths in the DCB test with: (a) composite skin; and (b) aluminium skin.

Also, the numerically calculated SERRs with respect to the crack length have been compared with those experimentally obtained in [46] for two types of DCB sandwich specimens denoted as 'thick DCB' and 'thin DCB'. All details concerning the tests may be obtained from the mentioned source and reference citations in that paper. The finite element predictions are quite close to the measured data over the entire range of crack length for both the specimens as seen in Fig. 16a and b. It is also obvious that the trends predicted by the finite element analysis are in a very good compliance with the experimental results. Based on the comparison between the FEM analysis and experiments, one can conclude that the computational models accurately represent the actual DCB fracture test.
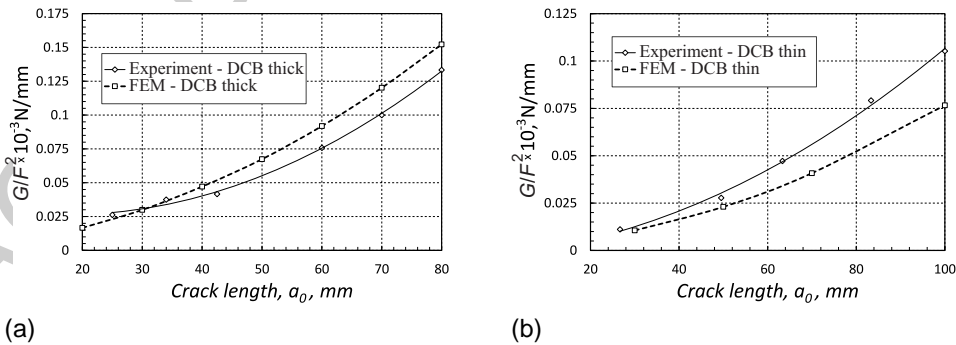

Figure 16: Comparison between numerical and experimental SERRs vs. crack length for DCB sandwich specimens: (a) thick sample; and (b) thin sample.

Further the influence of skin thickness (h_f) on the phase angle and the SERR in a DCB speci-
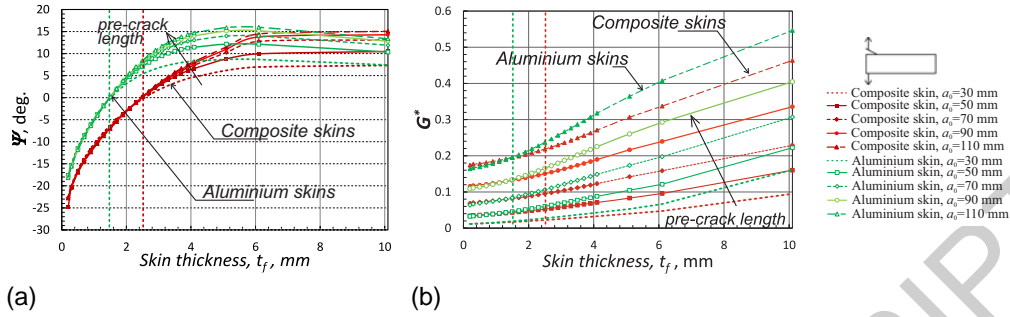
16

Figure 17: The variation of fracture parameters vs. the skin thickness t_f at different pre-crack lengths in the DCB test: (a) the phase angle $\hat{\psi}$ vs. t_f; and (b) the normalized SERR $\mathcal{G}^*$ vs. t_f.

men is studied using the finite element models validated above. The core modulus of E_c=80 MPa and the two types of skins (aluminium and composite) are used for this analysis. Fig. 17 displays the phase angle and the normalized SERR, $\mathcal{G}^*$, of the DCB specimens as functions of h_f for different lengths of initial debonding. One can see that unlike the SCB test coupons, the DCB specimens have both negative and positive values of the phase angle. The limited values of the skin thickness, splitting the DCB samples on two groups with respect to the phase angle sign, have been found approximately as $h_f = 1.5$ mm and $h_f = 2.5$ mm for aluminium and composite skins, respectively, as shown by the dash lines in Fig. 17a. The range of the phase angle values has been estimated to be from $-25°$ to $16°$ for composite skins and from $-18°$ to $17°$ for aluminium skins. Herewith, for very thin aluminium and composite skins the phase angle is negative with values close to those obtained in the SCB tests, but it takes positive values with increasing the skin thickness and these values are bigger for longer pre-cracks. Thus, there exist actual conditions that may cause kinking the debonding into the core material during the DCB test. Nevertheless, for the thicker skins, there are no significant quantitative changes in the phase angle with increasing the skin thickness as well as the difference between the phase angles of the two bi-material configurations decreases with increasing the skin thickness. Another interesting observation is that the phase angle is independent on pre-crack length for thin skins, i.e. when the bending stiffness of the upper skin is significantly smaller than bending stiffness of the rest specimen part (up to 2 mm for composite skins and up to around 3 mm for the stiffer aluminum skins). In this case, the phase angle takes negative or small positive values. By inspecting the plot of normalized SERR, Fig. 17b, one can see that the SERR increases with increasing the skin thickness and much more for longer pre-cracks especially for stiffer aluminium skins. Furthermore, the level of SERR in the DCB specimens is higher than that in the SCB samples of the same material configurations. An increase in the SERR indicates raising a mode II contribution during the DCB test. Also, all the graphs contain an initial weakly nonlinear region at thin composite and aluminium skins, followed by the linear range. Such the dependence contrasts with strongly linear one reported in the SCB specimens. Thus, unlike the SCB test, the DCB test method has less possibilities to realize the debonding in a mode I dominant regime by geometrical adjustments.

Nevertheless, the results shown in Fig. 18 reveal that the phase angle in the DCB test at each the skin thickness regardless the material combination has small sensitivity to the pre-crack length except for short pre-cracks at very thick skins, i.e. mode mixity holds nearly constant with the debonding growth for most the skin thicknesses at least for the range of pre-crack lengths
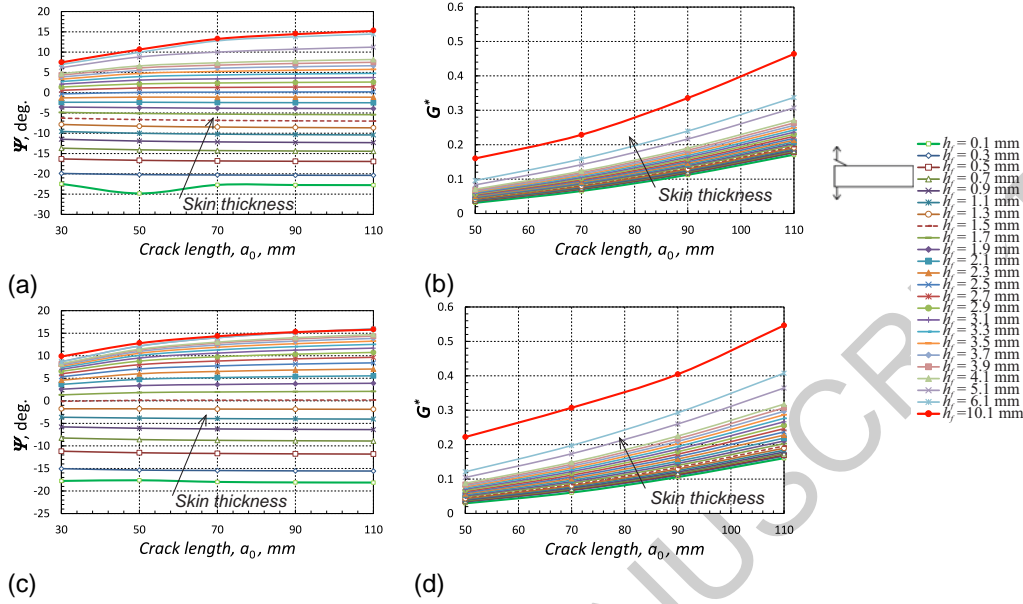
17

Figure 18: The variation of phase angle $\hat{\psi}$ and normalized SERR $\mathcal{G}^*$ vs. the pre-crack length a_0 at different skin thicknesses in the DCB test with: (a)-(b) composite skin; and (c)-(d) aluminium skin.

reported herein. This result appears to be almost identical to the findings observed in the SCB test. The SERR variations with increasing the initial crack at different skin thicknesses for both the skin materials exhibit also analogous trends to those discussed for the SCB specimens in Figs. 8b and 8d. However, in contrast to the latter, herein an increase in SERR is rather related to increasing the mode II component due to raising positive shear stresses in the vicinity of the crack tip than growing the mode I dominance. It follows from the fact of an increase of the mode II contribution into the phase angle and the SERR as observed earlier in Fig. 17.

Although the variations of the both fracture parameters in the DCB specimens with the composite skins and a stiffer core E_c =250 MPa with respect to skin thickness and pre-crack length demonstrate trends similar to those reported for the same samples with a low modulus core E_c =80 MPa, the quantitative differences between these two cases are substantial, as seen in Fig. 19a and 19b. In the case of stiffer core, the phase angle shifts into a new range $(-32°, 10°)$, where mode I dominant conditions occur mostly at thicker skins, i.e. at the skin thickness over 2.1 mm against 1.1 mm for the DCB samples with core modulus E_c =80 MPa. Furthermore, such the stiff-core specimens have a lower level of the SERR compared to the soft-core counterparts. This is identical to the SCB samples with a high modulus core (see Fig. 10a and 10b, respectively) and it is caused by smaller deformations of the stiffer specimens. Also, as seen in Fig. 19c and 19d, the phase angle of such the stiff-core DCB specimens is almost insensitive to the pre-crack lengths excluding short pre-cracks at very thick skins, and the SERR produced by the crack increases with increasing the pre-crack length and skin thickness. This is similar to the case of a low modulus core in Fig. 17.

The distribution of near-tip stress fields in the DCB sample with $a_0 = 50$ mm made of a low modulus core $E_c = 80$ MPa and the composite skins of the thickness of h_f =3.5 mm is demonstrated in Fig. 20. The computed fields of normal longitudinal and transversal stresses
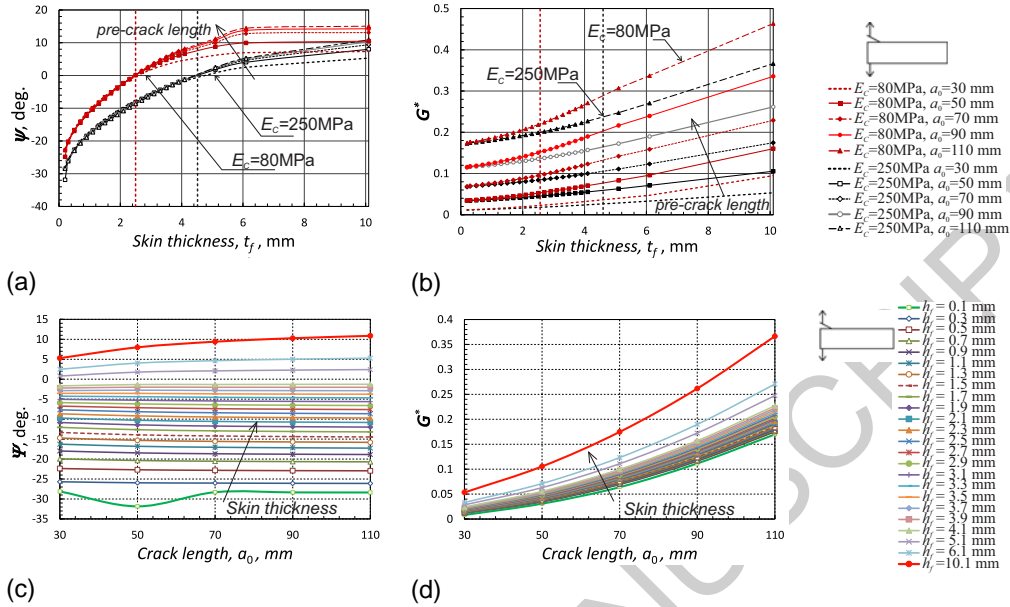
18

Figure 19: The variation of fracture parameters in the DCB specimen with composite skins and core modulus E_c=250 MPa: (a) the phase angle $\hat{\psi}$ vs. t_f; (b) the normalized SERR $\mathcal{G}^*$ vs. t_f; (c) the phase angle $\hat{\psi}$ vs. a_0; and (d) the normalized SERR $\mathcal{G}^*$ vs. a_0.

have profiles close to those (especially longitudinal stress) in the SCB specimen of the same materials, whereas the distribution of shear stress is completely different between the two samples (see Fig. 11). The reason of similarity is that the skins of both the specimens under the applied up-ward force behave in the same manner, but the difference in the shear stresses is due to an additional bending moment and shear force applied below the crack plane in the DCB sample. And, namely this feature common for all the DCB type specimens distinguishes them from the SCB ones. Hence, it is reasonable to expect that such the loading mechanism resulting in extra shear and normal stresses at the crack tip gives rise to a more complicated cracking behaviour in the DCB specimen. As seen in Fig. 20c, the shear stress in the vicinity of the crack tip of the DCB specimen is positive. This correlates with a negative phase angle in this test coupon at the analysed skin thickness as displayed in Fig. 17a. Thus, although the DCB specimen exhibits predominantly mode I regime at the given design, the crack will tend to grow towards rather the core material than the skin/core interface.

Finally, numerical analyses have been performed to investigate effects of the second pre-crack at the bottom skin/core interface in the DCB specimen on both the mode mixity and the total strain energy release rate. Fig. 21 presents such a sample with two interface cracks. The predicted variations of both the phase angle and the SERR with respect to the skin thickness are demonstrated in Fig. 22. One can see that the presence of the second debond has a profound effect on the fracture mechanics of the DCB specimen. At a short basic pre-crack ($a_0 = 50$ mm), the both fracture parameters are significantly affected by the existence of second pre-crack, Fig. 22a and 22b. Herewith, while the phase angle of the DCB specimens with a second crack of length up to 50 mm takes values smaller than those in the standard DCB test, it varies with increasing
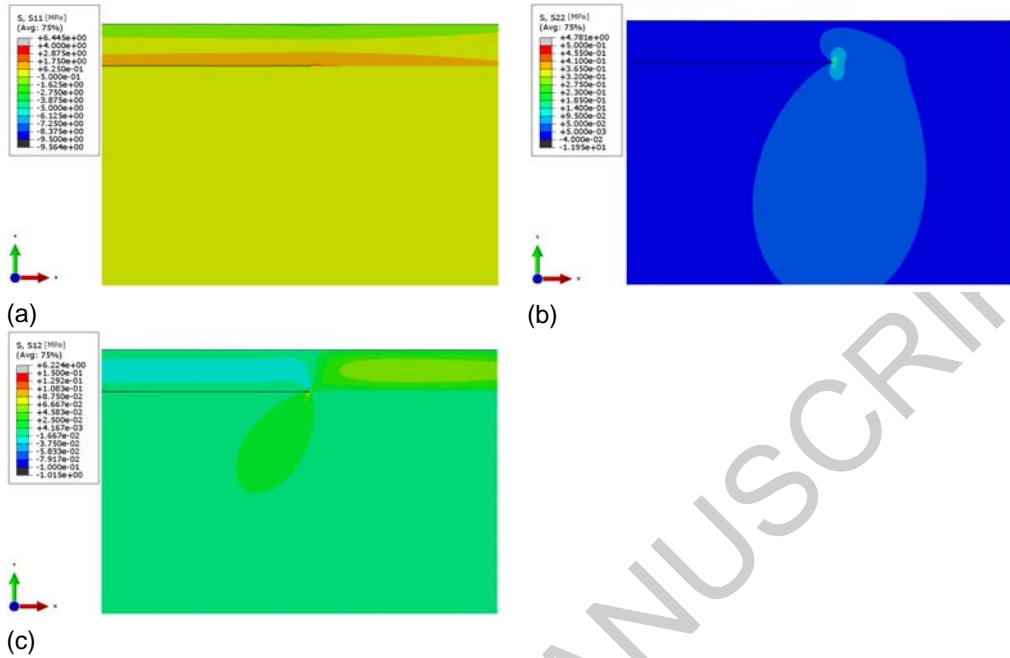
19

Figure 20: Stress distribution in front of the debonding in DCB specimen: (a) longitudinal normal stress σ_{11}; (b) transverse normal stress σ_{22}; and (c) in-plane shear stress σ_{12}.

the skin thickness similarly to the standard specimens. However, the situation completely is changed, when the length of second pre-crack becomes to be equal to the basic one. In this case, the phase angle moves to the negative range with drastic decreasing the mode I component, and growing the contribution of mode II. That is now the debonding is enforced to propagate towards the skin material. Also, the SERR of the samples with skin thicknesses over 2 mm drops more than two times compared to the standard test. The calculations for longer basic pre-cracks ($a_0 \geq 70$ mm) and the same range of second pre-crack lengths revealed a smaller sensitivity of the both estimated fracture parameters to the presence of a short second debond (< 50 mm) than in the previous case, but at $a_1 = 50$ mm the substantial changes similar to the results observed for the short basic pre-crack have been found as well, as seen in Fig. 22c-22d. It is evident that a second initial crack introduces additional flexibility, which leads to increasing the shear stress component. The longer the second pre-crack, the larger a shear component and, as a result, higher mode mixity and more deviation from the standard test conditions occur.

4. Conclusions

In the present work, the sandwich SCB and DCB specimens were examined from a mode I purity perspective by varying the skin thickness, initial debonding length and skin/core bi-material combination. The parametric studies were performed with the FEM code ABAQUS using two-dimensional models under plain strain conditions accurately reproducing the sandwich specimens, composed of two dissimilar linear materials. The mode I and mode II components of the complex SIF were extracted from the finite element solution by the integral interaction
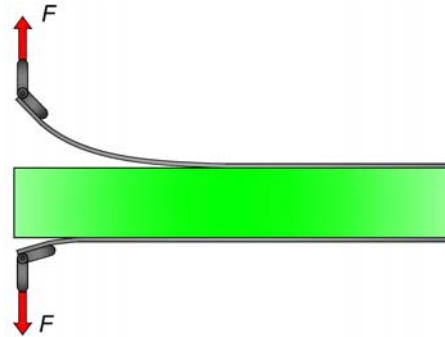
20

Figure 21: Sandwich Double Cantilever Beam test specimen with two debonds.

method and, then, mode mixity parameter and strain energy release rate were calculated by post-processing algorithms.

Using the simulations, it has been demonstrated that both the SCB and DCB specimens exhibit a strong sensitivity of the phase angle and the SERR to the variations in their geometrical and material parameters. However, in essence, the SCB specimens had better ability for testing the sandwich materials in mode I dominant conditions due to a wider range of the skin thicknesses and skin/core material combinations considered in the study, at which this regime could be sustained, and, also, due to somewhat more stability in the variation of the fracture parameters with respect to the local imperfections that may exist during testing in comparison to the DCB samples of the same geometry and materials. Also, in the SCB test method, it is paramount that the specimens induce only negative phase angle values, which decreases with increasing the skin thickness and this tendency holds over all the range of pre-crack lengths and material combinations. Unlike this, the DCB specimens produce both negative and positive phase angle values that leads to more limitations for interface crack propagation in mode I dominant regime. Furthermore, the positive phase angle even for the case of DCB sample design suitable for mode I dominance tends to kink the crack into the core material. That is extensive numerical simulations are needed till geometrical parameters at given material combinations are established for being used in real experimental testing.

Thereby, in line with the numerical observations made in the present study, careful selection of the SCB and DCB specimens is required to ensure that the fracture testing is conducted in the mode I regime at selected skin thicknesses and a skin/core material combination. The present work demonstrates a methodology that could be available for combining experimental and computational methods by means of computational framework.
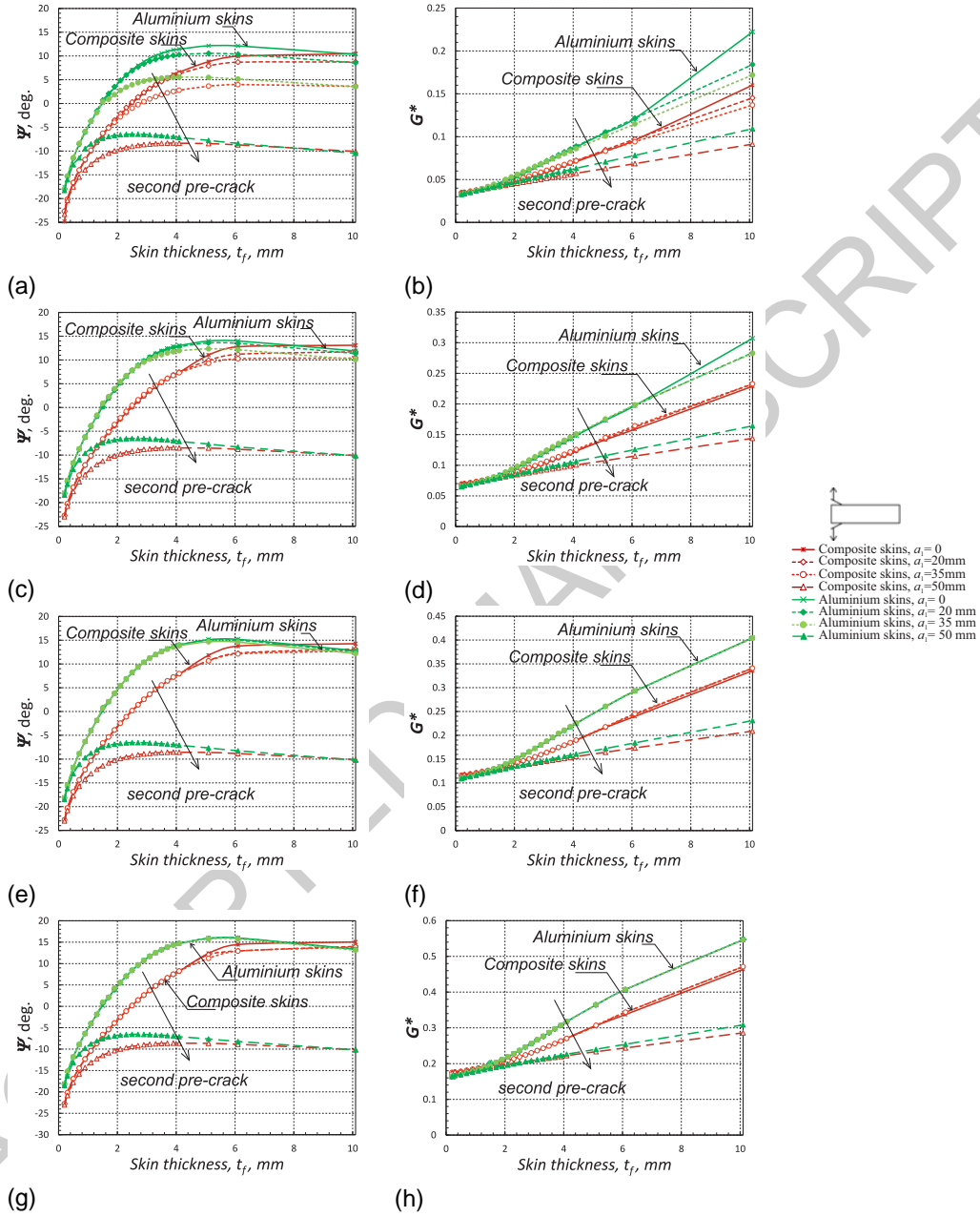
Acknowledgements

Figure 22: Comparisons of the phase angle and the normalized SERR vs. the skin thickness t_f between standard and modified DCB tests with composite and aluminium skins at different lengths of the second pre-crack a_1 in the case of basic pre-crack, a_0 equal to: (a)-(b) 50 mm; (c)-(d) 70 mm; (e)-(f) 90 mm; and (g)-(h) 110 mm.

22

References

[1] A. S. Herrmann, P. C. Zahlen, I. Zuardy, Sandwich structures technology in commercial aviation: Present applications and future trends, in: O. T. Thomsen, E. Bozhevolnaya, A. Lyckegaard (Eds.), Sandwich Structures 7 Advancing with Sandwich Structures and Materials, Netherlands: Springer, Dordrecht, 2005, p. 13–26.

[2] K. Branner, Capacity and lifetime of foam core sandwich structures, Ph.D. thesis, Department of Naval Architecture and Offshore Engineering, Technical University of Denmark, Lyngby, Denmark (1995).

[3] J. M. Gattas, Z. You, Design and digital fabrication of folded sandwich structures, Automation in Construction 63 (2016) 79–87.

[4] N. Z. M. Zaid, M. R. M. Rejab, N. A. N. Mohamed, Sandwich structure based on corrugated-core: A review, MATEC Web of Conferences 74, 6 pages.

[5] F. Ongaro, E. Barbieri, N. M. Pugno, Mechanics of mutable hierarchical composite cellular materials, Mechanics of Materials 124 (2018) 80–99.

[6] J.-S. Yang, L. Ma, R. Schmidt, G. Qi, Schröder, K.-U., J. Xiong, L.-Z. Wu, Hybrid lightweight composite pyramidal truss sandwich panels with high damping and stiffness efficiency, Composite Structures 148 (2016) 85–96.

[7] B. Han, K. Qin, B. Yu, B. Wang, Q. C. Zhang, T. Lu, Honeycomb–corrugation hybrid as a novel sandwich core for significantly enhanced compressive performance, Materials and Design 93 (2016) 271–282.

[8] B. Han, Z. J. Zhang, Q. C. Zhang, Q. Zhang, T. J. Lu, B. Lu, Recent advances in hybrid lattice-cored sandwiches for enhanced multifunctional performance, Materials and Design 10 (2017) 58–69.

[9] S.-S. Shi, Z. Sun, X.-Z. Hu, H.-R. Chen, Carbon-fiber and aluminum-honeycomb sandwich composites with and without kevlar-fiber interfacial toughening, Composite Part A 67 (2014) 102–110.

[10] I. Duarte, F. Teixeira-Dias, A. Graça, A. J. M. Ferreira, Failure modes and influence of the quasi-static deformation rate on the mechanical behavior of sandwich panels with aluminum foam cores, Mechanics of Advanced Materials and Structures 17 (5) (2010) 335–342.

[11] L. Marșavina, D. A. Șerban, C. Pop, R. Negru, Experimental investigation of failure modes for sandwich beams, in: Advances in Fracture and Damage Mechanics XVI, Vol. 754 of Key Engineering Materials, 2017, pp. 115–118.

[12] J. P. Vitale, G. Francucci, X. J., A. Stocchi, Failure mode maps of natural and synthetic fiber reinforced composite sandwich panels, Composites Part A 94 (2017) 217–225.

[13] M. Bîrsan, T. Sadowski, L. Marsavina, E. Linul, D. Pietras, Mechanical behaviour of sandwich composite beams made of foams and functionally graded materials, International Journal of Solids and Structures 50 (2013) 519–530.

[14] V. N. Burlayenko, T. Sadowski, Finite-element free vibration and buckling analyses of sandwich plates with honeycomb and foam cores, in: Proceedings of the 2nd International Conference Nonlinear Dynamics, NTU KhPI, Kharkiv, Ukraine, 2007, pp. 243–249.

[15] D. Elmalich, O. Rabinovitch, A high-order finite element for dynamic analysis of soft-core sandwich plates, Journal of Sandwich Structures and Materials 14 (5) (2012) 525–555.

[16] S. K. Sarangi, B. Basa, Nonlinear finite element analysis of smart laminated composite sandwich plates, International Journal of Structural Stability and Dynamics 14 (3), 29 pages.

[17] V. N. Burlayenko, H. Altenbach, T. Sadowski, An evaluation of displacement-based finite element models used for free vibration analysis of homogeneous and composite plates, Journal of Sound and Vibration 358 (8) (2015) 152–175.

[18] Z. Juhász, A. Szekrényes, Estimation of local delamination buckling in orthotropic composite plates using kirchhoff plate finite elements, Mathematical Problems in Engineering 2015 (Article 749607), 14 pages.

[19] R. Carrazedo, R. R. Paccola, H. B. Coda, Active face prismatic positional finite element for linear and geometrically nonlinear analysis of honeycomb sandwich plates and shells, Composite Structures 200 (2018) 849–863.

[20] V. N. Burlayenko, T. Sadowski, Effective elastic properties of foam-filled honeycomb cores of sandwich panels, Composite Structures 92 (2010) 2890–2900.

[21] E. I. S. Flores, F. A. DiazDelaO, M. I. Friswell, J. Sienz, A computational multi-scale approach for the stochastic mechanical response of foam-filled honeycomb cores, Composite Structures 94 (5) (2012) 1861–1870.

[22] A. Catapano, M. Montemurro, A multi-scale approach for the optimum design of sandwich plates with honeycomb core. part i: homogenisation of core properties, Composite Structures 118 (1) (2014) 664–676.

[23] P. Trovalusci, M. L. De Bellis, M. Ostoja-Starzewski, Generalized Continua as Models for Classical and Advanced Materials, Vol. 42 of Advanced Structured Materials, Switzerland: Springer, 2016, Ch. A statistically-based homogenization approach for particle random composites as micropolar continua, pp. 425–441.

[24] P. Trovalusci, M. L. De Bellis, R. Masiani, A multiscale description of particle composites: From lattice microstructures to micropolar continua, Composites Part B 128 (2017) 164–173.

[25] K. R. Pradeep, S. M. Srinivasan, B. Nageswara Rao, K. Balasubramaniam, Study on finite element modeling aspects of delaminated honeycomb sandwich beams, International Journal of Vehicle Structures and Systems 4 (3) (2012) 113–117.

23

[26] M. F. Funari, F. Greco, P. Lonetti, Sandwich panels under interfacial debonding mechanisms, Composite Structures 203 (2018) 310–320.

[27] A. Szekrényes, The role of transverse stretching in the delamination fracture of softcore sandwich plates, Applied Mathematical Modelling 63 (2018) 611–632.

[28] V. N. Burlayenko, T. Sadowski, Dynamic behaviour of sandwich plates containing single/multiple debonding, Computational Materials Science 50 (4) (2011) 1263–1268.

[29] V. N. Burlayenko, T. Sadowski, Shell-like Structures, Vol. 15 of Advanced Structured Materials, Berlin, Heidelberg: Springer, 2011, Ch. Dynamic analysis of debonded sandwich plates with flexible core – Numerical aspects and simulation, pp. 415–440.

[30] A. Szekrényes, Natural vibration-induced parametric excitation in delaminated kirchhoff plates, Journal of Composite Materials 50 (17) (2016) 2337–2364.

[31] I. N. Jayatilake, W. Karunasena, W. Lokuge, Finite element based dynamic analysis of multilayer fibre composite sandwich plates with interlayer delaminations, Advances in Aircraft and Spacecraft Science 3 (1) (2016) 15–28.

[32] Y. Qu, G. Meng, Nonlinear vibro-acoustic analysis of composite sandwich plates with skin-core debondings, AIAA Journal 55 (5) (2017) 1723–1733.

[33] T. Pölöskei, A. Szekrényes, Quasi-periodic excitation in a delaminated composite beam, Composite Structures 159 (2017) 677–688.

[34] V. N. Burlayenko, T. Sadowski, Linear and nonlinear dynamic analyses of sandwich panels with face sheet-to-core debonding, Shock and Vibration 2018 (Article 5715863), 26 pages.

[35] M. Idriss, A. El Mahi, Linear and nonlinear resonant techniques for characterizing cyclic fatigue damage in composite laminate, Composites Part B: Engineering 142 (2018) 36–46.

[36] V. N. Burlayenko, T. Sadowski, Numerical modeling of sandwich plates with partially dedonded skin-to-core interface for damage detection, in: G. D. Roeck, G. Degrande, G. Lombaert, G. Muller (Eds.), Proceedings of the 8th International Conference on Structural Dynamics EURODYN 2011, Leuven, Belgium, 2011, pp. 2242–2249.

[37] S. Mustapha, L. Ye, Non-destructive evaluation (NDE) of composites: assessing debonding in sandwich panels using guided waves, in: V. M. Karbhari (Ed.), Non-Destructive Evaluation (NDE) of Polymer Matrix Composites, Woodhead Publishing Ltd., 2013, pp. 238–278.

[38] A. Katunin, M. Chuda-Kowalska, Assessment of internal damages in sandwich panels via active thermography, Engineering Transactions 63 (2) (2015) 171–180.

[39] F. Seguel, V. Meruane, Damage assessment in a sandwich panel based on full-field vibration measurements, Journal of Sound and Vibration 417 (17) (2018) 1–18.

[40] Z. Juhász, T. Turcsán, T. B. Tóth, A. Szekrényes, Sensitivity analysis for frequency based prediction of crack size in composite plates with through-the-width delamination, International Journal of Damage Mechanics 27 (6) (2018) 859–876.

[41] J. Hutchinson, Z. Suo, Mixed mode cracking in layered materials, Advances In Applied Mechanics 29 (1991) 63–191.

[42] J. Rice, Elastic fracture mechanics concepts for interface cracks, Journal of Applied Mechanics 55 (1998) 98–103.

[43] D. O. Adams, J. Nelson, Z. Bluth, Development and evaluation of fracture mechanics test methods for sandwich composites, in: Proceedings of the 2012 Aircraft Airworthiness and Sustainment Conference, Baltimore, Md., 2012.

[44] X. Li, L. A. Carlsson, Elastic foundation analysis of tilted sandwich debond (tsd) specimen, Journal of Sandwich Structures & Materials 2 (1) (2000) 3–32.

[45] A. T. Nettles, Measuring core/facesheet bond toughness in honeycomb sandwich structures, Tech. rep., NASA/TP—2006–214713, Marshall Space Flight Center, Alabama (2006).

[46] F. Avilés, L. A. Carlsson, Analysis of the sandwich dcb specimen for debond characterization, Engineering Fracture Mechanics 75 (2008) 153–168.

[47] J. G. Ratcliffe, Sizing single cantilever beam specimens for characterizing facesheet/core peel debonding in sandwich structure, Tech. rep., NASA/TP–2010-216169, Langley Research Center, Hampton, Virginia (2010).

[48] P. Davidson, A. M. Waas, C. S. Yerramalli, Experimental determination of validated, critical interfacial modes i and ii energy release rates in a composite sandwich panel, Composite Structures 94 (2) (2012) 477 – 483.

[49] K. N. Shivakumar, H. Chen, S. A. Smith, An evaluation of data reduction methods for opening mode fracture toughness of sandwich panels, Journal of Sandwich Structures and Materials 7 (1) (2005) 77–90.

[50] M. Rinker, J. Ratcliffe, D. Adams, R. Kruger, Characterizing facesheet/core disbonding in honeycomb core sandwich structure, Tech. rep., NASA/CR-2013-217959, Langley Research Center, Hampton, Virginia (2013).

[51] P. Jolma, S. Segercrantz, C. Berggreen, Ultimate failure of debond damaged sandwich panels loaded with lateral pressure – an experimental and fracture mechanics study, Journal of Sandwich Structures and Materials 9 (2007) 167–196.

[52] I. V. Ivanov, Finite element analysis and modelling of active fibre composites including damages, Computational Materials Science 50 (4) (2011) 1276 – 1282.

24

[53] V. N. Burlayenko, T. Sadowski, Modeling of the dynamic debonding growth of sandwich plates, in: Y. V. Mikhlin, N. V. Perepelkin (Eds.), Proceedings of the 4th International Conference on Nonlinear Dynamics ND-KhPI 2013, NTU KhPI, Tochka Publ., Sevastopol, Ukraine, 2013, pp. 225–230.

[54] V. N. Burlayenko, T. Sadowski, Simulations of post-impact skin/core debond growth in sandwich plates under impulsive loading, Journal of Applied Nonlinear Dynamics 3 (4) (2014) 369–379.

[55] V. N. Burlayenko, T. Sadowski, D. Pietras, A numerical analysis of near tip fields in a bending moment-loaded double cantilever sandwich beam fracture specimen, Bulletin of NTU KhPI: Mathematical modelling in engineering and technology 3 (1279) (2018) 9–14.

[56] ABAQUS, User's manual, ver. 2016, Dassault Systémes Simulia Corp., Providence, RI, USA (2016).

[57] Z. Suo, J. Hutchinson, Sandwich test specimens for measuring interface crack toughness, Materials Science and Engineering: A 107 (1989) 135–143.

[58] F. H. K. Chen, R. T. Shield, Conservation laws in elasticity of the j-integral type, Zeitschrift für angewandte Mathematik und Physik 28 (1) (1977) 1–22.

[59] C. F. Shih, R. J. Asaro, Elastic-Plastic Analysis of Cracks on Bimaterial Interfaces: Part I—Small Scale Yielding, Journal of Applied Mechanics 55 (2) (1988) 299–316.

[60] D. M. Parks, The virtual crack extension method for nonlinear material behavior, Computer Methods in Applied Mechanics and Engineering 12 (3) (1977) 353–364.

[61] S. Natarajan, C. Song, S. Belouettar, Numerical evaluation of stress intensity factors and t-stress for interfacial cracks and cracks terminating at the interface without asymptotic enrichment, Computer Methods in Applied Mechanics and Engineering 279 (2014) 86–112.

[62] G. Anlas, M. Santare, J. Lambros, Numerical calculation of stress intensity factors in functionally graded materials, International Journal of Fracture 104 (2) (2000) 131–143.

25